ORIGINAL PAPER

Determination of adenosine triphosphate based on the use of fluorescent terbium(III) organic frameworks and aptamer modified gold nanoparticles

Chao Sun [1,2,3] · Shiyu Zhao [4] · Fei Qu [1,2] (iD) · Wenli Han [5] · Jinmao You [1,2,6]

Abstract
A thiol-labeled adenosine triphosphate (ATP) binding aptamer is covalently linked on the surface of gold nanoparticles (AuNPs). This warrants protection of the red AuNPs from aggregation in high salt condition. The dispersed AuNPs can quench the fluorescence of the Tb(III)-MOFs at 547 nm with the excitation wavelength of 290 nm. This is ascribed to the combined action of inner filter effect, dynamic quenching and fluorescence resonance energy transfer. If the aptamer binds ATP to form folded structures, the AuNPs aggregate in high salt medium and the green fluorescence of the Tb(III)-MOFs is recovered. This method shows good sensitivity and selectivity for ATP, and the linear range is from 0.5 to 10 μM of ATP with the detection limitat of 0.32 μM. It was applied to the determination of ATP in (spiked) human plasma with satisfactory recoveries (from 93.2% to 106.3%). Oppositely, when the unlabeled aptamer is used instead of thiol-labeled aptamer in this process, the ATP-aptamer complexes rather than unlabeled aptamer provide greater protection for AuNPs against salt-induced aggregation. It is found that when the aptamer covalently binds to AuNPs, the steric hindrance is dominant for the stabilization of AuNPs; for unlabeled aptamer, the electrostatic repulsion is responsible for their stability, irrespective of whether ATP is present or not. These two different forces lead to the aggregation or dispersion of AuNPs with addition of target in salt solution.

✉ Fei Qu
qufei3323@163.com

✉ Wenli Han
0904hanwenli@163.com

1 The Key Laboratory of Life-Organic Analysis, Qufu Normal University, Qufu 273165, Shandong, China

2 The Key Laboratory of Pharmaceutical Intermediates and Analysis of Natural Medicine, Qufu Normal University, Qufu 273165, Shandong, China

3 Beijing Key Laboratory of Photoelectronic/Electrophotonic Conversion Materials, Key Laboratory of Cluster Science, Ministry of Education, School of Chemistry and Chemical Engineering, Beijing Institute of Technology, Beijing 100081, China

4 Dalai Nur Sub-bureau of Hulunbuir Ecology and Enviroment Bureau, Dalai Nur District, Hulunbuir 021410, Inner Mongolia, China

5 Laboratory Animal Center, Chongqing Medical University, Chongqing 400016, China

6 Key Laboratory of Tibetan Medicine Research & Qinghai Provincial Key Laboratory of Tibetan Medicine Research, Northwest Institute of Plateau Biology, Chinese Academy of Science, Xining 810001, China

Introduction

Adenosine triphosphate (ATP) is regarded as the primary energy currency, has a significant effect on regulating various biochemical reactions, and also plays a vital role in diagnosing diseases [1]. Considering the importance of ATP in biological determination, exploring a reliable and specific method for monitoring of ATP is highly encouraging. Studies about the determination of ATP usually take advantage of aptamer features in terms of high affinity and good selectivity. Typically, two different aptamers are concerned: one is the label-free aptamer and the other one is the thiol-modified aptamer (SH-aptamer). The label-free aptamer-based approaches are usually convenient and cheap, but the thiol-modified aptamer can be immobilized on a gold electrode or Au nanoparticles (AuNPs) though covalent bond to form a stable signal source [2, 3]. Especially for AuNPs, they can interact with unlabeled aptamer through van der Waals forces and react with thiol-modified aptamer via gold-sulfur bond [4, 5]. However, it's unknown for the effects of these two different interactions on the detection of the same substance.

Besides, as a significant branch of metal-organic frameworks (MOFs), lanthanide metal-organic frameworks (Ln-MOFs), are porous crystalline materials formed by the coordination of organic ligands and lanthanide ions [6]. Owing to their intriguing structural diversity and outstanding characteristics, Ln-MOFs have been extensively researched in a variety of applications such as gas storage [7], separation [8], catalysis [9] and sensors [10]. In the application of luminescent detection, the intrinsic luminescent properties, including bright visible emission, narrow emission band and large Stokes shift, make the Ln-MOFs excellent candidates for the design of novel sensors [11]. Among the attractive Ln(III) ions, Tb^{3+} ion is one of the most extensively utilized for constructing fluorescent MOFs. It can coordinate with organic ligands to produce the characteristic green emissions through the ligand-to-Tb^{3+} ion energy transfer [12]. During the past few years, the Tb-MOFs sensors have been widely investigated for cations [13], anions [14], nitroaromatic compounds [15] and so on. Owing to the enriched electrons of ligands, a great majority of sensing mechanisms can be ascribed to the photoinduced electron transfer (PET), where Tb-MOFs act as an electron donor. For example, the nitrobenzene explosives with electron-deficient group such as 2,4,6-trinitrophenol (TNP), 4-nitrophenol (4-NP), 2-nitrophenol (2-NP), nitrobenzene (NB) and 2,4-dinitrotoluene (2,4-DNT), can obtain electrons from the excited state of ligands of MOFs leading to the luminescence quenching [16]. The process of PET requires that the energy level of lowest unoccupied molecular orbital of the ligand should be higher than that of targets [17]. While most of biomolecules, such as DNA, enzyme and protein, are electron-rich substances, it limits their detection by PET

sensing mechanism. Thus, it is still a great challenge to further explore biomolecules using Tb-MOFs as a platform. Compared with the PET, both fluorescence resonance energy transfer (FRET) and inner filter effect (IFE) are highly popular mechanisms in determining analytes that are closely related to human life [18]. However, to the best of our knowledge, there is few report involving luminescent Tb-MOFs concentrating on FRET and IFE for sensing biomolecules.

In our previous report [19], it was found that the fluorescence of Tb-MOFs was quenched by the dispersed AuNPs rather than these aggregated ones. Thiolated ATP binding aptamer (SH-ABA) is covalently linked on the surface of AuNPs (SH-AuNPs), which can keep dispersing well in high salt solution and quench the emissions of Tb-MOFs. However, when the complexes of SH-ABA and ATP form, they cannot protect AuNPs in high salt solution, resulting in the aggregation of AuNPs and the fluorescence recovery of Tb-MOFs. Therefore, a fluorescent aptasensor for ATP is constructed based on the interaction between Tb-MOFs and SH-AuNPs. The linear range of ATP is from 0.5 to 10 μM with the limit of detection (LOD) of 0.32 μM. It is applied to the detection of ATP in (spiked) human plasma with satisfactory recoveries. Interestingly, while the unlabeled aptamer is used instead of thiol-labeled one, the ATP-aptamer complexes rather than unlabeled aptamer provide greater protection for AuNPs. The opposite phenomena arouse our great interest in investigating the influence of these two strategies on the detection of ATP. It is found that the different repulsive forces (steric repulsion and electrostatic repulsion) between AuNPs and thiol-labeled or unlabeled aptamer lead to the aggregation or dispersion of AuNPs with addition of target in salt solution. This is the first investigation focused on the impact of the repulsive forces between AuNPs and aptamer on the detection of target. The results may be beneficial for widen the applications of sensing through combination of new fluorescent materials, AuNPs and aptamer.

Experiment section

Reagents and chemicals

Terbium(III) chloride hexahydrate (TbCl$_3$·6H$_2$O), N, N-dimethylformamide (DMF), sodium citrate, chloroauric acid (HAuCl$_4$·4H$_2$O), Tween 20, Tris (hydroxymethyl) amino methane (Tris), ATP, adenosine monophosphate (AMP), adenosine diphosphate (ADP), cyclic adenosine monophosphate (c-AMP), guanosine triphosphate (GTP), uridine triphosphate (UTP) and cytidine triphosphate (CTP) were purchased from Aladdin (Shanghai, China, http://www.aladdin-e.com). The 5′-thiol-modified aptamer of ATP (5'-SH-(CH$_2$)$_6$-ACC TGG GGG AGT ATT GCG GAG GAA GGT-3′, SH-ABA) was synthesized and purified from Sangon

Biotechnology Co., Ltd. (Shanghai, China, http://www.sangon.com). 3, 5-Dicarboxybenzeneboronic acid (5-bop) was purchased from HWRK Chemicals Co., Ltd. (Beijing, China, http://mall.hwrkchemical.com/). The ATP enzyme-linked immunosorbent assay (ELISA) kit was purchased from Jiangsu Baolai Biotechnology Co., LTD. (Yancheng, China, http://www.jsmlsw.com/). HCl, HNO_3 and NaCl were purchased from Shenbo Chemical Co., Ltd. (Shanghai, China, http://www.shenbohg.com/). All reagents were of analytical grade and without additional purification. Ultrapure water was utilized throughout the experiments.

Instrumentation and characterization

The fluorescence emission were recorded by Hitachi F-7000 fluorescence spectrophotometer (Tokyo, Japan) equipped with a quartz cell (1 cm × 1 cm) in the emissions mode. The ultraviolet-visible (UV-vis) absorption spectra were collected on a Cary 300 Bio UV-vis spectrophotometer. The transmission electron microscopy (TEM) images were taken on a JEM-2100PLUS (JEOL, Japan) and the dynamic light scattering (DLS) experiments were carried out with ALV 500 laser light scattering instrument. The Fourier transform infrared (FTIR) spectrum was recorded from Thermo Nicolet Nexus 470 FT-IR ESP spectrometer. The X-ray diffraction (XRD) spectrum was performed using MiniFlex600 X-ray powder diffractometer. The pH values of solutions were measured using a pH meter (MettlerToledo FE20, Switzerland). The fluorescence decay curves were obtained by a photo-counting system from Quantaurus-Tau C11367–11 (Hamamatsu) with laser excitation at 290 nm. Zeta potential was measured using a Zetasizer Nano ZS-90 (Malvern Instruments, Malvern, UK).

Preparation of Tb-MOFs, AuNPs, and aptamer-modified AuNPs

The Tb-MOFs were synthesized by the solvothermal reaction as described in previous literature [20]. The AuNPs were prepared by the citrate reduction method [21], and thiolated aptamer of ATP were attached to AuNPs according to a reported method [22]. More details about the synthesis of the materials are presented in the Electronic Supporting Material.

Fluorometric assay of ATP

Firstly, 150 μL mixtures of SH-AuNPs conjugates and different concentrations of ATP were placed in EP tubes at room temperature for 40 min. The solution of SH-AuNPs contained 25 mM Tris-HCl (pH 7.4), 150 mM NaCl. Then, the mixtures were equilibrated for another 30 min by the addition of 87.5 μL NaCl (4 M). Next, 20 μL Tb-MOFs (0.4 mg·mL^{-1}) was added into the above solution with a final volume of 1 mL

for another 5 min prior to fluorescent measurements. Upon excitation at 290 nm, the fluorescence spectra were collected followed by analysis of the emissions at 547 nm. Furthermore, the change of fluorescence intensity was calculated according to $F-F_0$, where F and F_0 represented the intensities of the mixture at 547 nm in the presence and absence of ATP, respectively.

Determination of ATP in human plasma

Firstly, 1.0 mL blood sample was kept at 37 °C in a water bath for about 0.5 h. Then, the sample was deproteinized with addition of acetonitrile (mixture of human plasma and acetonitrile at a 1:2 ratio) by centrifugation at 4000 rpm (3800×g) for 20 min. Following by keeping in a water bath to evaporate acetonitrile, the supernatant was collected and diluted to 100 times by deionized water before use. Finally, three different concentrations (3, 5 and 8 μM) of standard ATP were spiked into the deproteinized human plasma and quantified by the present sensing system.

Results and discussion

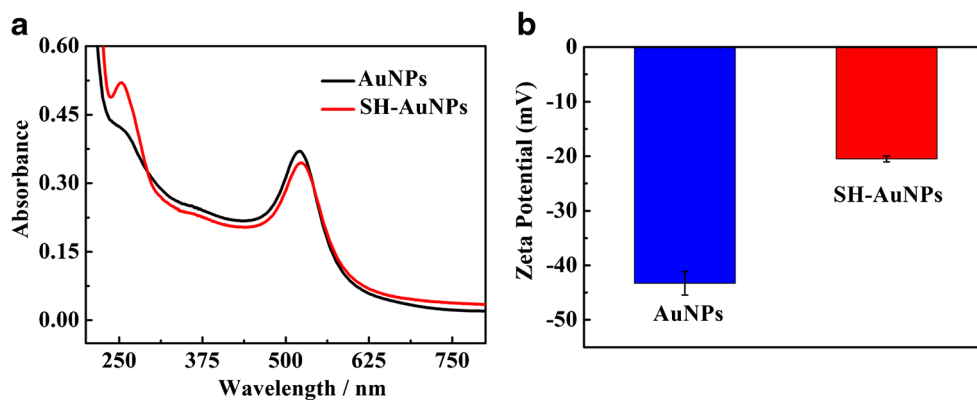### The characterization of Tb-MOFs and of gold nanoparticles modified with aptamer (SH-AuNPs)

The fluorescence spectra of Tb^{3+} ions and free ligand (5-bop) as well as Tb-MOFs are measured in ambient temperate (Fig. 1a). Upon excitation at 290 nm, the Tb^{3+} ions exhibit weak fluorescence due to f-f forbidden transitions, and free ligand shows a strong emission at 447 nm. When Tb-MOFs are formed, the efficient energy transfer from ligand to the Tb^{3+} center occurs, which is often called the antenna effect [23], accompanying with the emission disappearance of the free ligand. Thus, Tb-MOFs exhibit characteristic enhanced emission peaks at 492, 547, 587 and 623 nm, which are designated to the $^5D_4$-^7F_J (J = 6, 5, 4, 3) transitions of the Tb^{3+} ions, respectively [24]. The prominent emission peaks of Tb-MOFs at 492 nm and 547 nm make it visually bright green under UV lamp (inset, Fig. 1a), which are recorded for further study. Figure 1b shows the homogeneously bar morphology of Tb-MOFs with well-dispersion in water carried out by TEM experiment. DLS analysis is conducted to obtain the average hydrodynamic diameter (D_h) of the Tb-MOFs, which is about 583.8 nm (Fig. S1a). As confirmed by FT-IR spectra, the peak of ligand at 1704 cm^{-1} is the C=O stretching vibration ($\nu_{C=O}$), but disappears in Tb-MOFs, proving that carboxylate groups of ligand coordinate with Tb^{3+} to construct Tb-MOFs (Fig. S1b). The PXRD pattern of Tb-MOFs is in good agreement with the simulated one, indicating the successful synthesis of Tb-MOFs (Fig. S1c).

Fig. 1 a Fluorescence spectra of free terbium ions, free ligand (5-bop) and Tb-MOFs with excitation at 290 nm, and the insets are photographs of Tb-MOFs under UV light at 254 nm and daylight; b TEM image of Tb-MOFs
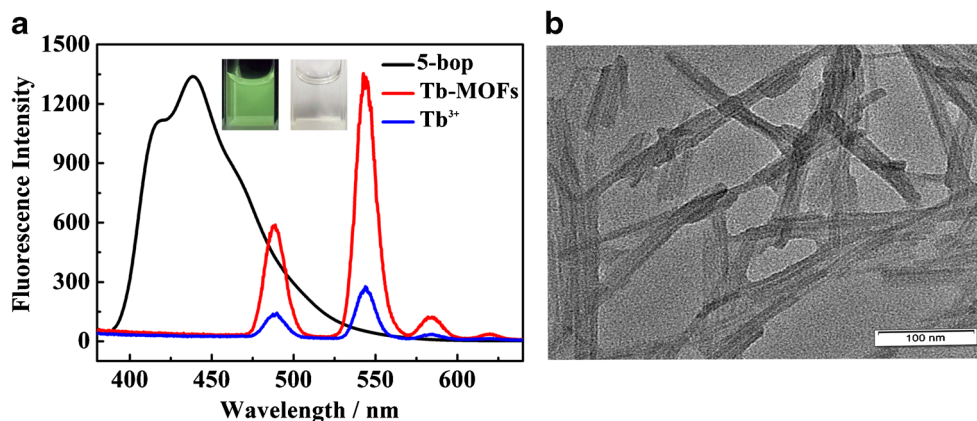
When the 5′-thiol-modified aptamer (SH-ABA) covalently binds with AuNPs to form SH-AuNPs through thiol-gold bonding, the absorption peak of SH-AuNPs at 523 nm shows a little reduction and exhibit a new absorption band at about 258 nm compared with bare AuNPs (Fig. 2a). TEM image reveals that spherical morphology and size of SH-AuNPs are similar to the free AuNPs (Fig. S2a), and the SH-AuNPs are uniform with the average diameter of 19.1 ± 0.80 nm (Fig. S2b). The Dh of SH-AuNPs is about 39.98 nm which is larger than AuNPs because SH-ABA is attached to the surface of AuNPs (Fig. S2c). In addition, SH-AuNPs is −20.5 mV in the absence of salt, and they are less negatively charged than bare AuNPs (Fig. 2b). These results suggest SH-aptamer is successfully immobilized on the surface of AuNPs. Besides, salt tolerance assay (Fig. S3) suggests that SH-AuNPs can keep dispersed even in the 500 mM NaCl. Although unlabeled ABA can stabilize AuNPs against salt-induced aggregation to a certain extent compared with bare AuNPs, these particles still agglomerate significantly when NaCl further increases to 100 mM. The results demonstrate that the covalently linked SH-aptamer on the surface of AuNPs can provide a more extraordinary stabilization effect than the unlabeled aptamer. However, the thiol-labeled aptamer is more expensive than unlabeled one and the modification of aptamer onto the AuNPs is also complex and time-consuming [25]. Thus, this sometimes limits the application of labeled strategy.

The quenching mechanism of Tb-MOFs by SH-AuNPs

As previously mentioned [19], the fluorescence of Tb-MOFs was quenched effectively by the dispersed AuNPs, while the quenching ability of aggregated AuNPs was small (Fig. S4). Similarly, the dispersed SH-AuNPs can also quench the fluorescence of Tb-MOFs. The fluorescence of Tb-MOFs decreases gradually with increasing the concentration of SH-AuNPs; when the concentration of SH-AuNPs is 2 nM, the fluorescence of Tb-MOFs approximately drops to 76% (Fig. 3).

The quenching mechanism of Tb-MOFs by SH-AuNPs has been investigated in detail. As displayed in Fig. 4a, there is a large overlap region between the absorption spectrum of dispersed SH-AuNPs (in the range of 200–600 nm) and the fluorescence excitation/emission spectra of Tb-MOFs (λex = 290 nm, λem = 547 nm). While the SH-AuNPs aggregate, the absorption peak of these particles at 520 nm fades down and red shifts to 680 nm resulting in less overlap region. Therefore, the dispersed SH-AuNPs induced fluorescence suppression of Tb-MOFs is first presumed to the IFE. To verify this hypothesis, corrections are investigated by taking into consideration the cuvette geometry used in the fluorescence measurements and the absorption characteristics of the aqueous solution according to the Eq. 1 [26]:

Fig. 2 a Comparison of UV-vis absorption spectra and (b) zeta potentials of bare AuNPs and SH-AuNPs

Fig. 3 a Fluorescence spectra of Tb-MOFs upon addition of various concentrations of SH-AuNPs and (**b**) the corresponding quenching efficiency. All data are recorded at the emission of 547 nm with the excitation at 290 nm
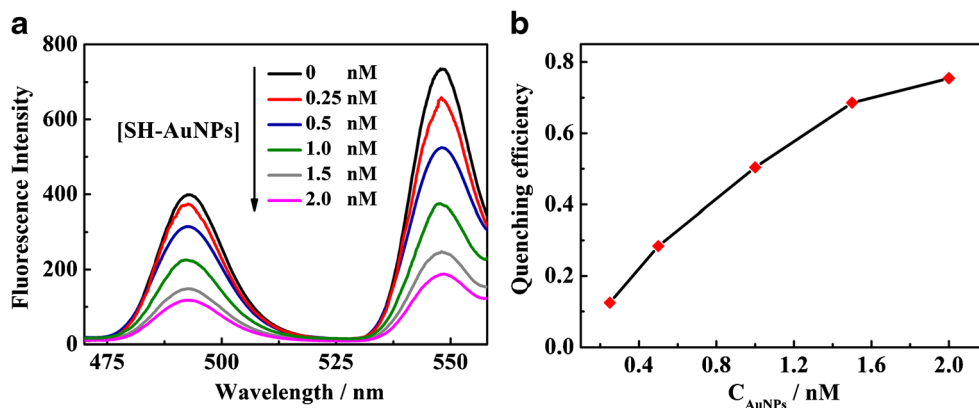
$$\frac{Fcor}{Fobsd} = \frac{2.3dAex}{1-10^{-dAex}}10^{gAem}\frac{2.3sAem}{1-10^{-sAem}} = CF \quad (1)$$

where F_{obsd} represents the observed fluorescence intensity of Tb-MOFs with the introduction of SH-AuNPs and F_{cor} is the corrected fluorescence intensity by removing IFE from F_{obsd} ($\lambda em = 547$ nm); A_{ex} and A_{em} refer to the absorbance of Tb-MOFs with the addition of SH-AuNPs at 290 nm (corresponding to excitation wavelength) and 547 nm (corresponding to emission wavelength). Geometry parameters of d, g and s are 1, 0.4 and 0.1 cm, respectively. What's more, the correction factor (CF) of IFE cannot exceed 3, otherwise the correction is not convincing.

The CF of IFE at each concentration of SH-AuNPs is calculated in Table S1. After removing the IFE from the totally observed suppressed fluorescence, the suppressed efficiency for the totally observed (E_{cor}) and the corrected (E_{obsd}) fluorescence of Tb-MOFs are figured out in Fig. 4b, as described in Eqs. 2 and 3.

$$E_{obsd} = 1 - F_{obsd}/F_{obsd,0} \quad (2)$$

$$E_{cor} = 1 - F_{cor}/F_{cor,0} \quad (3)$$

where $F_{obsd,0}$ and $F_{cor,0}$ refer to the fluorescence intensity and

the corrected fluorescence intensity of the Tb-MOFs in the absence of SH-AuNPs. It can be observed that about 16% of quenching effect can be ascribed to IFE at 298 K. This result suggest some other quenching mechanism coexisting.

Apart from IFE, fluorescence quenching effect usually involves static quenching effect (SQE) or dynamic quenching effect (DQE) or both of them. By using Stern-Volmer Eq. 4 [27], the role of SQE and DQE in fluorescence suppression can be evaluated,

$$\frac{F_0}{F} = 1 + Ksv[Q] \quad (4)$$

where F and F_0 are the corrected fluorescence intensities of Tb-MOFs in the presence and absence of the SH-AuNPs according to Eq. 1 (giving in Table S1), respectively; [Q] is the concentration of SH-AuNPs and K_{SV} is the Stern-Volmer constant. Fig. S5 displays that all the Stern-Volmer plots at different temperate show good linear relationships, which is generally indicative of a single predominant type of SQE or DQE in this process [28]. The fluorescence lifetime is a significant factor, and it keeps constant for SQE with the addition of the quencher, but changes in DQE [29]. It can be observed that the fluorescence lifetime of Tb-MOFs declines from 5.8 to 4.1 ns when SH-AuNPs are added (Fig. S6), revealing that the
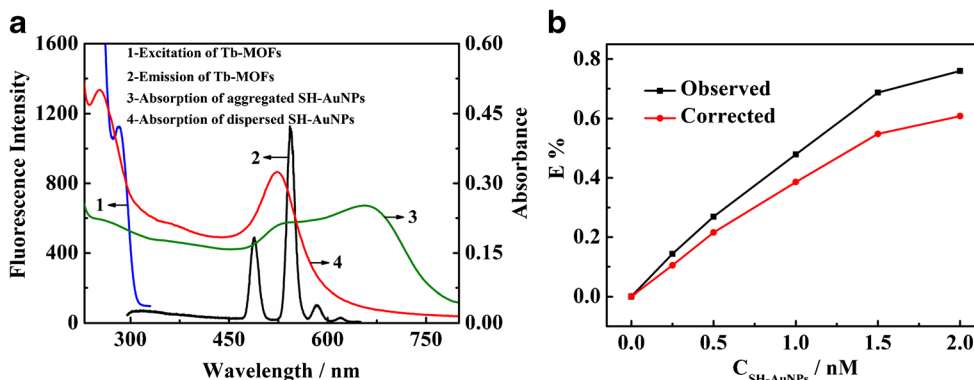
Fig. 4 **a** Spectral overlap between the UV-vis absorption spectra of dispersed and aggregated SH-AuNPs with fluorescence excitation and emission spectra of Tb-MOFs ($\lambda ex = 290$ nm, $\lambda em = 547$ nm); **b** Observed and corrected suppressed efficiency of Tb-MOFs with addition of various concentrations of SH-AuNPs. The data are recorded at the emission of 547 nm with the excitation at 290 nm

remaining fluorescence quenching may be mainly caused by DQE rather than SQE. The Stern-Volmer slopes of plots rise with increasing temperature (Fig. S5), also indicating that the quenching process may be mainly a dynamic quenching mechanism.

As well known, the fluorescence lifetime remains almost constant by IFE but varies in FRET process [30]. Additionally, the emission spectrum of Tb-MOFs overlaps well with absorption spectrum of dispersed SH-AuNPs. Hence, the role of FRET in the entire suppression process is also studied. The major difference between IFE and FRET is the requirement of the close proximity between energy donor and acceptor for FRET [31]. It can be clearly seen in Fig. S7a that the zeta potential of Tb-MOFs is 24.8 mV and SH-AuNPs are −20.5 mV. The electrostatic interaction between the positively charged Tb-MOFs and the negatively charged SH-AuNPs can bring them closer to meet the donor-acceptor distance demand of the FRET. In addition, TEM image also verifies that negatively charged SH-AuNPs are evenly distributed on the bar morphology of Tb-MOFs (Fig. S7b). Thus, all these proofs reveal that quenching mechanism can be assumed to be the synergistic effect of IFE, DQE and FRET.

Determination of ATP based on the Tb-MOFs@SH-AuNP system

As depicted in Fig. 5, compared with the characteristic emissions at 492 and 547 nm of Tb-MOFs, 5′-thiol-modified aptamer (SH-ABA) and free ATP do not interfere with the emissions of Tb-MOFs (curve 1, 2, 3). However, SH-AuNPs can maintain dispersed in high salt condition, resulting in the fluorescence of Tb-MOFs quenching (curve 4). In the presence of ATP, the SH-ABA covalently linked on the surface of AuNPs can specifically capture ATP to form complexes,
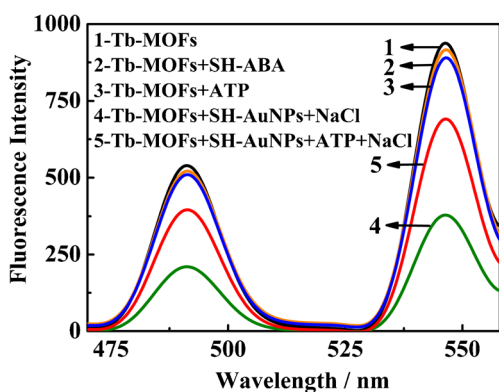
Fig. 5 Fluorescence spectra of Tb-MOFs in the absence (curve 1) and presence of 5′-thiol-modified aptamer (SH-ABA) (curve 2), ATP (curve 3), the mixture of SH-AuNPs and 350 mM NaCl (curve 4) and the mixture of SH-AuNPs, ATP and 350 mM NaCl (curve 5). The SH-ABA, SH-AuNPs, NaCl and ATP are 30 nM, 1.5 nM, 350 mM and 10 μM respectively. All data are recorded at the emission of 547 nm with the excitation at 290 nm

causing a conformational change from random coil to the folded structure. The analysis of zeta potential in Fig. S8 reveals that the potential of SH-AuNPs is −10.7 mV in high NaCl solution which is less negative than SH-AuNPs alone (−20.5 mV) due to the neutralization of NaCl. After the addition of ATP, the potential of the complexes formed by SH-ABA and ATP is further reduced (−7.3 mV). Owing to the loss of electrostatic stabilization, it can be clear seen in TEM images (Fig. S9) that these SH-AuNPs aggregate significantly with addition of targets in high salt condition. The Dh of these particles increases from 39.9 to 1084.0 nm (Fig. S10), also invalidating the agglomeration of these particles. Thus, the fluorescence recovery of Tb-MOFs is observed in the presence of SH-AuNPs and ATP due to the aggregation of these nanoparticles (curve 5, Fig. 5). By virtue of the dispersion/aggregation of SH-AuNPs modulated by the target, the novel Tb-MOFs@SH-AuNPs platform is established for the determination of ATP. To improve the sensitivity of ATP detection, the experiment conditions including the concentration of NaCl and SH-ABA as well as the reaction time are optimized (Fig. S11), and the detail is described in Electronic Supporting Material.

Under optimum conditions, the Tb-MOFs@SH-AuNPs system is applied for quantitative determination of ATP. With the increasing concentration of ATP, SH-AuNPs gradually aggregate, causing the fluorescence recovery of Tb-MOFs. As is shown in Fig. 6, the enhancement of fluorescent signal of Tb-MOFs is proportional to the concentration of ATP in the range from 0.5 to 10 μM. The limit of detection is estimated to be 0.32 μM on the basis of the 3σ/slope (σ represents the standard deviation of the blank samples).

Selectivity

In order to evaluate the selectivity of this method, some analogous molecules such as GTP, CTP, UTP, ADP, AMP and c-AMP are tested. As is shown in Fig. 7, the addition of target ATP results in the dramatic recovery efficiency of Tb-MOFs, whereas only a slight change can be observed in the presence of 10 times of the above-mentioned species. Thus, these ATP analogues have no obvious interference and this method exhibit good selectivity due to the high specific recognition of ATP by SH-ABA.

Analysis of real samples

The ATP concentration in human plasma samples has been detected based on this method. However, it should be mentioned that the excitation of Tb-MOFs (λex = 290 nm) is in the UV range, so the UV light used for fluorescence excitation will be screened off by UV absorbers in plasma and this will weaken the signal. When the plasma samples are diluted 100-fold, matrix effects are negligible on the emissions of
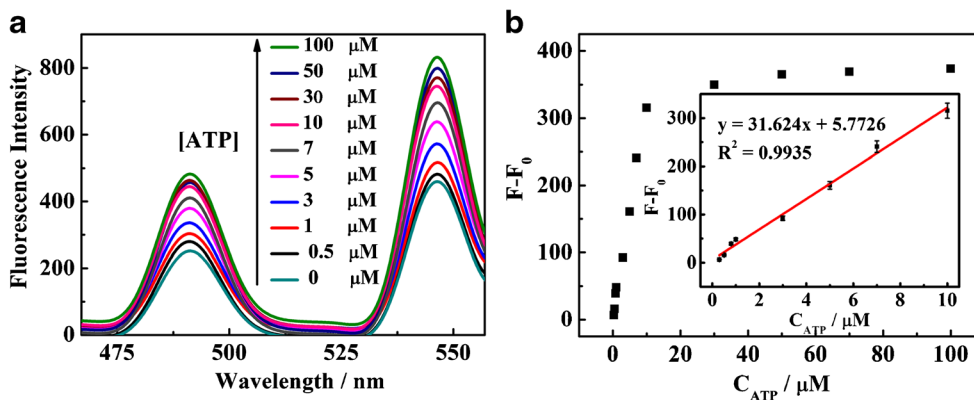
Fig. 6 a Fluorescence spectra of Tb-MOFs@SH-AuNPs system in the presence of different concentrations of ATP and (**b**) corresponding linear range. The concentrations of SH-AuNPs and NaCl are 1.5 nM and 350 mM, respectively. All data are recorded at the emission of 547 nm with the excitation at 290 nm

Tb-MOFs. A range of diseases such as cardiovascular, Parkinson's and Alzheimer's diseases can lead to excessive production of ATP [32]. Therefore, the method of standard additions is used to assess the practicality of this method in real samples. With addition of different amounts of ATP into the spiked plasma samples, the desirable recoveries from 93.2% to 106.3% are obtained with the relative standard deviation (RSD) lower than 1.9% (Table S2). ELISA is adopted as an independent analytical method for ATP and there is no significant difference between the ELISA and the method, indicating the reliability of this strategy. The aptasensor can be applied for the quantitative screening of ATP in complex biological fluids.

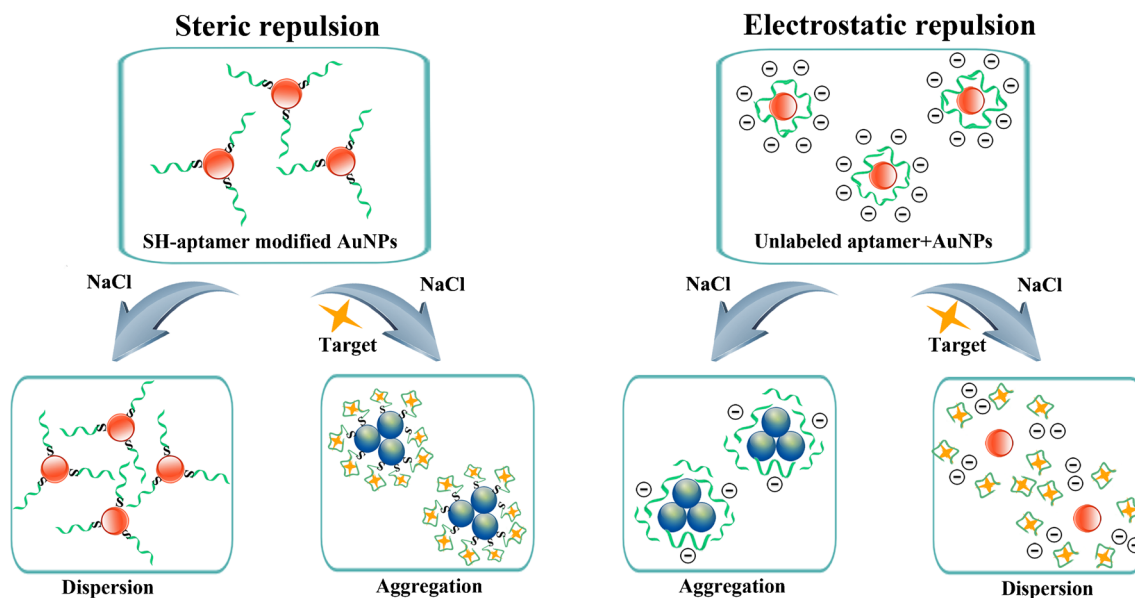## The repulsive forces between AuNPs and thiolated/unlabeled aptamer

The DNA can protect AuNPs against salt-induced aggregation through multiple forces which are critical factors for AuNPs stabilization, including van der Waals force, electrostatic repulsion and steric repulsion. As illustrated in Scheme 1, when
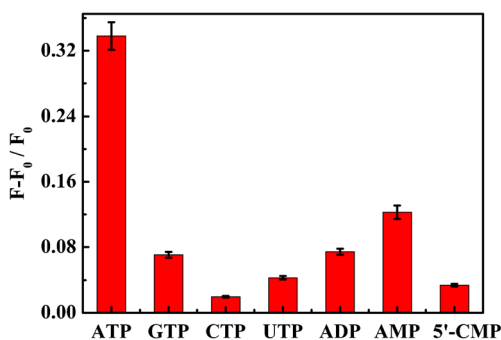
Fig. 7 Selectivity of Tb-MOFs@SH-AuNPs system for the detection of ATP (5 μM) against other control analogous molecules, GTP, CTP, UTP, ADP, AMP and c-AMP (50 μM). The concentrations of SH-AuNPs and NaCl are 1.5 nM and 350 mM, respectively. All data are recorded at the emission of 547 nm with the excitation at 290 nm

SH-labeled ABA is covalently linked on the surface of AuNPs by Au-S bonds, the long chain and random coil structure of DNA may increase steric hindrance between inter-particles. These SH-AuNPs show less negative charge (−20.5 mV) than AuNPs alone (−43.3 mV), but these nanoparticles still have better salt tolerance than free AuNPs in high salt concentration (Fig. S3). This indicates that steric hindrance is dominant for stabilization of SH-AuNPs. With addition of ATP, because of specific recognition between aptamer and target, some aptamer-target complexes form with a folded structure, so the repulsive force between these particles reduces. Moreover, these SH-AuNPs combined ATP show less negative potential (−7.3 mV). Therefore, both electrostatic and steric repulsion forces decrease leading to the aggregation of SH-AuNPs in high salt condition. It means that AuNPs covalently linked by aptamer are stable in high salt conditions (350 mM), but aggregate after adding targets.

However, when the unlabeled ABA is utilized instead of SH-ABA, it is interesting that the opposite phenomena occur. In Fig. S12, the unlabeled ABA can not protect AuNPs in 100 mM NaCl leading to the aggregation of these particles. While in the presence of target ATP, ABA specific binds to ATP to form complexes and they can protect AuNPs efficiently. The interaction between the unlabeled aptamer and AuNPs mainly relies on the van der Waals force and electrostatic repulsion. In comparison of AuNPs with ABA (−47.3 mV), the surface charge of AuNPs is less negative after addition of NaCl (−26.4 mV) due to the neutralization of the opposite-charge species (Fig. S13). Therefore, the electrostatic repulsion is the significant factor for label-free DNA to stabilize AuNPs. However, when the unlabeled ABA binds to ATP by converting to a folded structure, the negative charge of AuNPs with these folded aptamers increase to −28.5 mV. This result is consistent with the previous literature report [25], and supports the hypothesis [33] that the folded structure provides an electric double layer on the surface of AuNPs. Hence, a

Scheme 1 Schematic illustration of the repulsive forces (electrostatic repulsion and steric repulsion) of AuNPs and thiolated/unlabeled aptamer AuNPs

unique colloidal stabilization effect towards AuNPs is obtained. The different protection ability of unlabeled aptamer and aptamer-target complexes toward AuNPs can also be employed to modulate the fluorescence signal change of Tb-MOFs (Fig. S14), and the detailed experiments and discussions have been reported by our previous work [19].

In summary, when the aptamer covalently binds to AuNPs, steric hindrance is dominant for the stabilization of AuNPs. For unlabeled aptamer, the electrostatic repulsion is always responsible for maintaining AuNPs stability whether target exists or not. These two different forces lead to the aggregation or dispersion of AuNPs with addition of target in salt solution.

Conclusion

Based on the interaction between dispersed SH-AuNPs and Tb-MOFs, an aptamer-based method is constructed and applied to the sensitive and selective detection of ATP. The quenching mechanisms by SH-AuNPs towards Tb-MOFs are ascribed to IFE, DQE and the FRET. Most importantly, steric hindrance plays a crucial role in stabilizing AuNPs immobilized the thiol-labeled aptamer, while the electrostatic repulsion is dominant when free AuNPs interact with unlabeled aptamer. This study may help us to have a more clear understanding of the interaction between aptamer and AuNPs, and offers a new concept to fabricate the sensing platform through combination of new fluorescent materials, AuNPs and aptamer.

Author contribution Chao Sun and Shiyu Zhao contributed equally to this work.

Compliance with ethical standards

Conflict of interest The authors declare that they have no conflict of interest.

Ethical committee approval The human plasma sample experiments were performed with the approval of the Guidelines for Ethical Committee, Qufu Normal University. All plasma samples were from health volunteers with their informed consent. All studies were approved by Ethical Committee, Qufu Normal University.

References

1. Zheng FF, Zhang PH, Xi Y, Chen JJ, Li LL, Zhu JJ (2015) Aptamer/graphene quantum dots nanocomposite capped fluorescent mesoporous silica nanoparticles for intracellular drug delivery and real-time monitoring of drug release. Anal Chem 87(23):11739–11745
2. Liu Y, Lei J, Huang Y, Ju H (2014) "Off-on" electrochemiluminescence system for sensitive detection of ATP via target-induced structure switching. Anal Chem 86(17):8735–8741
3. Chen SJ, Huang YF, Huang CC, Lee KH, Lin ZH, Chang HT (2008) Colorimetric determination of urinary adenosine using

aptamer-modified gold nanoparticles. Biosens Bioelectron 23(11): 1749–1753

4. Peng Y, Li LD, Mu XJ, Guo L (2013) Aptamer-gold nanoparticle-based colorimetric assay for the sensitive detection of thrombin. Sensors Actuators B Chem 177:818–825

5. Yao W, Wang L, Wang H, Zhang X, Li L (2009) An aptamer-based electrochemiluminescent biosensor for ATP detection. Biosens Bioelectron 24(11):3269–3274

6. Wang LD, Wang SX, Chen Y (2017) Detection of cyanide via extended Π-conjugation-induced fluorescence enhancement of a metal organic framework composed of terbium(III), bipyridyl and adenosine diphosphate. Microchim Acta 184:4597–4602

7. Li XY, Li YZ, Yang Y, Hou L, Wang YY, Zhu ZH (2017) Efficient light hydrocarbon separation and CO_2 capture and conversion in a stable MOF with oxalamide-decorated polar tubes. Chem Commun 53(96):12970–12973

8. Li YZ, Wang HH, Yang HY, Hou L, Wang YY, Zhu ZH (2018) An uncommon carboxyl-decorated metal-organic framework with selective gas adsorption and catalytic conversion of CO_2. Chem-Eur J 24(4):865–871

9. Chen QQ, Cheng JH, Wang J, Li L, Liu ZP, Zhou XH, You YJ, Huang W (2019) A fluorescent Eu (III) MOF for highly selective and sensitive sensing of picric acid. Sci China Chem 62(2):205–211

10. Dai Y, Zhang JJ, Liu SQ, Zhou H, Sun YJ, Pan YZ, Yang JS, Ni J, Yang JS (2018) A trichromatic and white-light-emitting MOF composite for multi-dimensional and multi-response ratiometric luminescent sensing. Chem-Eur J 24(38):9555–9564

11. Zhao J, Wang YN, Dong WW, Wu YP, Li DS, Zhang QC (2016) A robust luminescent Tb (III)-MOF with Lewis basic pyridyl sites for the highly sensitive detection of metal ions and small molecules. Inorg Chem 55(7):3265–3271

12. Ji GF, Liu JJ, Gao XC, Sun W, Wang JZ, Zhao SL, Liu ZL (2017) A luminescent lanthanide MOF for selectively and ultra-high sensitively detecting Pb^{2+} ions in aqueous solution. J Mater Chem A 5(21):10200–10205

13. Zhou XH, Cheng JH, Li L, Chen Q, You YJ, Xiao HP, Huang W (2018) A europium (III) metal-organic framework as ratiometric turn-on luminescent sensor for Al^{3+} ions. SCI China Mater 61(5):752–757

14. Yao ZQ, Li GY, Xu J, Hu TL, Bu XH (2018) A water-stable luminescent Zn^{II} metal-organic framework as chemosensor for high-efficiency detection of Cr^{VI}-anions ($Cr_2O_7^{2-}$ and CrO_4^{2-}) in aqueous solution. Chem-Eur J 24(13):3192–3198

15. Zhou XH, Li L, Li HH, Li A, Yang T, Huang W (2013) A flexible Eu (III)-based metal–organic framework: turn-off luminescent sensor for the detection of Fe (III) and picric acid. Dalton T 42(34):12403–12409

16. Lin XM, Niu JL, Lin J, Hu L, Zhang G, Cai YP (2016) A luminescent Tb (III)-MOF based on pyridine-3,5-dicarboxylic acid for detection of nitroaromatic explosives. Inorg Chem Commun 72:69–72

17. Wu S, Lin Y, Liu J, Shi W, Yang G, Cheng P (2018) Rapid detection of the biomarkers for carcinoid tumors by a water stable luminescent lanthanide metal–organic framework sensor. Adv Funct Mater 28(17):1707169

18. Medintz IL, Clapp AR, Mattoussi H, Goldman ER, Fisher B, Mauro JM (2003) Self-assembled nanoscale biosensors based on quantum dot FRET donors. Nat Mater 2(9):630–638

19. Qu F, Sun C, Lv XX, You JM (2018) A terbium-based metal-organic framework@ gold nanoparticle system as a fluorometric probe for aptamer based determination of adenosine triphosphate. Microchim Acta 185(8):359

20. Yang ZR, Wang MM, Wang XS, Yin XB (2017) Boric-acid-functional lanthanide metal-organic frameworks for selective ratiometric fluorescence detection of fluoride ions. Anal Chem 89(3):1930–1936

21. Kimling J, Maier M, Okenve B, Kotaidis V, Ballot H, Plech A (2006) Turkevichmethod for gold nanoparticle synthesis revisited. J Phys Chem B 110:15700–15707

22. Xie S, Qiu L, Cui L, Liu H, Sun Y, Liang H, Chen Z (2017) Reversible and quantitative Photoregulation of target proteins. Chem 3(6):1021–1035

23. Abdelhamid HN, Bermejo-Gómez A, Martín-Matute B, Zou X (2017) A water-stable lanthanide metal-organic framework for fluorimetric detection of ferric ions and tryptophan. Microchim Acta 184(9):3363–3371

24. Cai D, Guo H, Wen L, Liu C (2013) Fabrication of hierarchical architectures of Tb-MOF by a "green coordination modulation method" for the sensing of heavy metal ions. Cryst Eng Comm 15(34):6702–6708

25. Huo Y, Qi L, Lv XJ, La T, Zhang J, Zhang ZQ (2016) A sensitive aptasensor for colorimetric detection of adenosine triphosphate based on the protective effect of ATP-aptamer complexes on unmodified gold nanoparticles. Biosens Bioelectron 78:315–320

26. Gauthier TD, Shane EC, Guerin WF, Seitz WR, Grant CL (1986) Fluorescence quenching method for determining equilibrium constants for polycyclic aromatic hydrocarbons binding to dissolved humic materials. Environ Sci Technol 20(11):1162–1166

27. Han YX, Chen YL, Liu JJ, Niu XY, Ma YX, Ma SD, Chen XG (2018) Room-temperature synthesis of yellow-emitting fluorescent silicon nanoparticles for sensitive and selective determination of crystal violet in fish tissues. Sensor Actuat B-Chem 263:508–516

28. Qu F, Ding YR, Lv XX, Xia L, You JM, Han W (2019) Emissions of terbium metal–organic frameworks modulated by dispersive/agglomerated gold nanoparticles for the construction of prostate-specific antigen biosensor. Anal Bioanal Chem 411(17):3979–3988

29. Li N, Liu SG, Dong JX, Fan YZ, Ju YG, Luo HQ, Li NB (2018) Using high-energy phosphate as energy-donor and nucleus growth-inhibitor to prepare carbon dots for hydrogen peroxide related biosensing. Sensor Actuat B-Chem 262:780–788

30. Guo JJ, Li HK, Xue M, Zhang MW, Cao XY, Luo YL (2014) Highly sensitive detection of organophosphorus pesticides represented by methamidophos via inner filter effect of au nanoparticles on the fluorescence of CdTe quantum dots. Food Anal Methods 7(6):1247–1255

31. Zhang J, Zhou R, Tang D, Hou X, Wu P (2018) Optically-active nanocrystals for inner filter effect-based fluorescence sensing: achieving better spectral overlap. Trac-Trend Anal Chem 110:183–190

32. Gourine AV, Llaudet E, Dale N, Spyer KM (2005) ATP is a mediator of chemosensory transduction in the central nervous system. Nature 436(7047):108–111

33. He F, Tang Y, Wang S, Li Y, Zhu D (2005) Fluorescent amplifying recognition for DNA G-quadruplex folding with a cationic conjugated polymer: a platform for homogeneous potassium detection. J Am Chem Soc 127(35):12343–12346